Author: Verdolini, Silvia
Title: Modeling interstellar bubbles : near and far
Issue Date: 2014-02-20

IV

A study of H II regions in NGC 6822 and the distribution of star-forming galaxies in emission line diagnostic diagrams

Derivation of physical parameters of H II regions, such as age, radius and density of the ambient medium, is important in understanding the interaction of massive stars with their surroundings, the mechanisms driving the expansion of the ionized gas, and the link between star forming galaxies and single H II regions. We seek to obtain well constrained physical parameters of H II regions in the nearby universe and use such information to understand the star forming sequence of Sloan Digital Sky Survey (SDSS) galaxies in optical line diagnostic diagrams and their relation with single H II regions. We select two well-studied H II regions in the nearby galaxy NGC 6822: Hubble V and Hubble X. We collect archive data: optical emission line images, optical photometry, and infrared (IR) data. We make use of unidimensional analytical models to constrain the density of the medium around each H II region. We carry out photoionization models of H II regions powered by stellar winds and radiation pressure. We find that the ambient densities derived from analytical expansion models are generally higher than observations suggest. We are able to confirm the young age of the cluster and the ionization state of the region. We compare with a selection of SDSS galaxies and find that their emission characteristics are consistent with most of their light coming from the few brightest H II regions rather than the most dim ones.The location of Hubble V and Hubble X on the BPT diagram confirms the evolutionary tracks derived from the photoionization models. The two H II regions represent the low end of the distribution of star forming galaxies. Analysis of our models shows that the most massive stellar cluster in blue star forming galaxies tend to be younger than our H II regions.

Silvia Verdolini, Lynn R. Carlson, Sherry C. C. Yeh, Maud Galametz, Vianney Lebouteiller, Jarle Brinchmann, Frédéric Galliano, Alexander G. G. M. Tielens
to be submitted

4.1 Introduction

Detailed studies of H II regions in the local universe are important in understanding star formation processes, the evolution of high mass stars, and properties of the interstellar medium (ISM) in which they expand. When a high mass star emits radiation, the gas around it becomes ionized. The ionized gas is heated by photoelectrons and and cooled through line emission processes, primarily, optical forbidden lines and IR fine structure lines from trace species. For a constant density nebula, the resultant H II region's size (the Strömgren radius) can be derived from the global ionization balance which equates the total photon luminosity from the star with the total recombination rate integrated over the nebula.

The Baldwin et al. (1981) diagram (hereafter the BPT diagram) is a commonly used tool to study extragalactic H II regions and their host galaxies. The most used combination is [O III] $\lambda5007$/Hβ versus [N II] $\lambda6584$/Hα that, in the galactic context, allows a clear distinction between star-forming and AGN dominated galaxies. In this plot, single H II regions cover a narrow sequence that overlaps with the star-forming sequence of the Sloan Digital Sky Survey (SDSS) galaxies (Brinchmann et al. 2004). The location on this sequence is controlled by physical properties of the H II region, such as metallicity, density of the ISM, ionization parameter, and age. Understanding how the star forming sequence is connected to single H II regions on the BPT diagram can be helpful to assess physical properties of unresolved H II regions in extragalactic galaxies. Models of the BPT diagram, or in general any line emission, are produced using photoionization model codes such as Cloudy (Ferland et al. 2013) or MAPPINGS III (Sutherland & Dopita 1993, Dopita et al. 2000). It is possible to create a set of predicted H II regions' line emission that can be compared to the observed BPT diagram for a set luminosity of the central star or star cluster, density of the ambient medium, and age. Such modeling is important in understanding H II regions' structures and in constraining their physical properties. By matching observations and a grid of models on the BPT diagram, it is possible to derive an approximate cluster age and ionization state of the region, even if the region is unresolved.

Observationally, H II regions have complex structures, and it is sometimes difficult to disentangle physical parameters making it problematic to compare with theoretical models. Recently, variations of the principal emission line ratios and derived physical values within H II regions have been found by studying giant H II regions and large star-forming regions in nearby galaxies using integral field spectroscopy. Such studies include H II regions in the outer disk of NGC 6946 at a distance of 5.9 Mpc (García-Benito et al. 2010), and N588 (Monreal-Ibero et al. 2011), N595 (Relaño et al. 2010), and IC132 and the central region (López-Hernández et al. 2013) of M33 at a distance of 840 kpc. Many studies of closer H II regions, such as 30 Doradus in the Large Magellanic Cloud (50 kpc) (Lopez et al. 2011, Pellegrini et al. 2011), have shown the level of complexity that can be reached in one single star forming region including multiple star formation events at different ages and locations, triggered star formation, and colliding stellar winds.

The aim of this study is to investigate the properties of H II region and compare observations with theory. We select two well-studied H II regions that have available multi-wavelength observations of gas and dust. They are two bright, single, resolved extragalactic H II regions Hubble V and Hubble X in the Local Group dwarf irregular NGC 6822. In term of size, stellar cluster, and density, we expect that those two H II regions are much better analogues of H II regions dominating the emission of SDSS galaxies than either galactic compact H II regions such as Orion or M17 or the intense starburst associated with 30 Dor in the Large Magellanic Cloud. Indeed, the distance of NGC 6822 (490 kpc; Mateo 1998), provides good spatial resolution compared to other extragalactic sources. It is the closest active star forming galaxy after the Magellanic System (Cannon et al. 2012) and the closest with no massive neighbor. It is gas-rich and has a metallicity of $Z \sim 0.4\ Z_{\odot}$. A large neutral gas disk has been reported by de Blok & Walter (2000), and it shows a complicated structure of shells and holes indicating a past interaction event (Cannon et al. 2012). Hubble V and Hubble X are two of its most prominent star forming regions and have similar ionizing clusters and ages but different morphologies. Hubble V is more compact, while Hubble X displays an almost spherical shell, typical of idealized H II regions. O'Dell et al. (1999) studied the ionization properties of the two regions from optical emission-line images. Bianchi et al. (2001) used Hubble Space Telescope (HST) imaging to derive resolved stellar photometry and study the high mass stars contained in the two clusters, showing that both H II regions contain very young stellar populations and several massive stars.

The structure of the paper is as follows. In Section 2, we describe the data used for the analysis. In Section 3, we compare theoretical models of the expansion of H II regions with the observations. In Section 4 we present our photoionization models. We discuss our findings in Section 5, and we finish with conclusions in Section 6.

4.2 Data set

4.2.1 Optical emission line images

Optical emission line images come from the Wide Field Planetary Camera 2 (WFC2) from the HST and are taken from the Hubble Legacy Archive (HLA). Bands used are F487N ($H\beta$), F502N [O III], F656N ($H\alpha$), and F658N [N II]. These Level 2 combined images were fully reduced by the HLA team using the IRAF[1] package MultiDrizzle and are provided by HLA in units of electrons/second. We convert to W m^{-2} by multiplying by the PHOTFLAM keyword provided in the fits image header and by the central wavelength. Original images were taken as part of Program GTO 6159 and presented by O'Dell et al. (1999).

We use high resolution optical imaging to examine the morphology and determine the radius of the H II regions. Hubble V consists of two separate structures: a very bright core in all emission lines powered by a compact stellar cluster consisting of a few OB stars as identified via photometry (see Section 4.2.2) and an extended structure towards the South-East powered by less massive B stars. We focus our study only on the bright core which we refer to as Hubble V for the rest of the paper. We adopt a radius for Hubble V of

[1] IRAF is distributed by the National Optical Observatories, which are operated by AURA Inc., under cooperative agreement with the National Science Foundation.

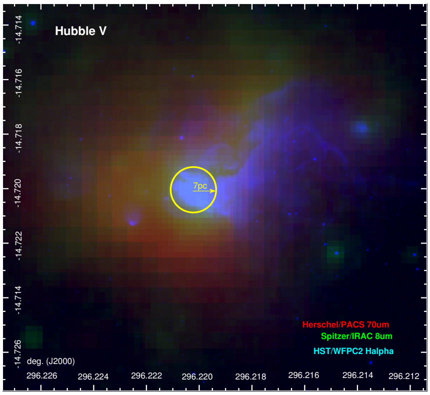

Figure 4.1 – Composite image of Hubble V: HST F656N (Hα) tracing hot ionized gas (blue); *Spitzer*/IRAC 8 μm showing PAH emission and tracing the photodissociation region (green) and *Herschel*/PACS 70 μm tracing denser gas of the molecular cloud (red). The circle indicates the selected area for the analysis done in the rest of this paper. Intensities are shown on a logarithmic scale.

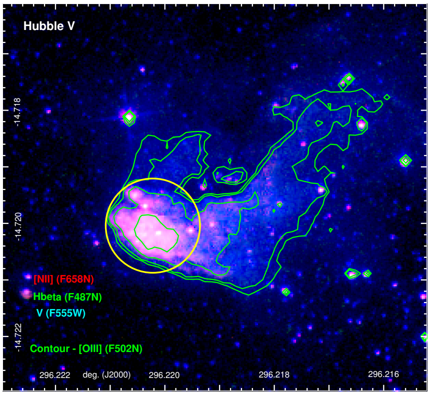

Figure 4.2 – Zoomed-in composite image of Hubble V: HST F555W-V band (blue) showing the stars of the cluster. HST F487N Hβ (green); HST F658N [N II] (red); and contours for HST F502N [O III]. The circle indicates the selected area for the analysis done in the rest of this paper. Intensities are shown on a logarithmic scale.

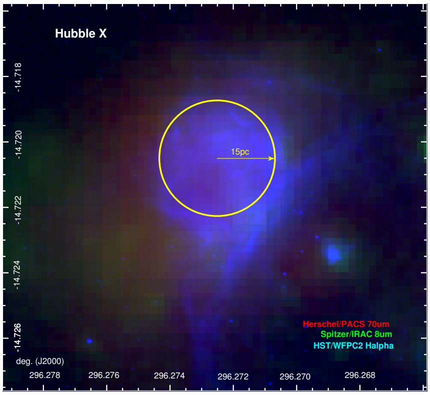

Figure 4.3 – Composite image of Hubble X: HST F656N (Hα) tracing hot ionized gas (blue); *Spitzer*/IRAC 8 μm showing PAH emission and tracing the photodissociation region (green) and *Herschel*/PACS 70 μm tracing denser gas of the molecular cloud (red). The circle indicates the selected area for the analysis done in the rest of this paper. Intensities are shown on a logarithmic scale.

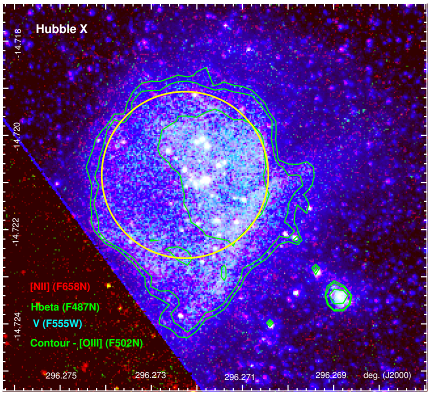

Figure 4.4 – Zoomed-in composite image of Hubble X: HST F555W-V band (blue) showing the stars of the cluster. HST F487N Hβ (green); HST F658N [N II] (red); and contours for HST F502N [O III]. The circle indicates the selected area for the analysis done in the rest of this paper. Intensities are shown on a logarithmic scale.

7 pc. Figure 4.1 shows Hα emission together with *Spitzer* and *Herschel* (Section 4.2.3). Hα traces the wall inside the H II region, surrounded by a photodissociation region and the parent molecular cloud, traced by *Spitzer* and *Herschel* respectively. In Figure 4.2 we illustrate the other strong line emission, together with the V band. All the brightest emission is located within the 7 pc radius.

Figure 4.3 and 4.4 show that Hubble X has a more spherical shape, close to the ideal H II region, and it is more extended. It has a radius of ~ 15 pc centered on the stellar cluster visible in the V band. The Hα image shows that at the South-East of the main bubble there is an arch-like diffuse emission. We believe that this structure is the remains of an old H II region, confirmed by the considerably older age of the stellar content of this region. Towards the South-East of the image there is another isolated clump, bright in all line emission, a separate small H II region with its own population of massive stars. We will refer to Hubble X as only the region within the marked radius.

4.2.2 Optical photometry

Bianchi et al. (2001) constructed the H-R diagram for star-forming regions in NGC 6822, including Hubble V and X, using HST UBV photometry. They superimpose isochrones from the model atmospheres of Bertelli et al. (1994) and derive ages of the stellar population < 4 Myr for both star forming regions. Although there are a few evolved stars in their H-R diagrams, they are simply looking over a larger field of view; those sources lie outside of the physical structures we examine here.

We use photometry provided in Massey et al. (2007) to characterize the stellar population. Observations were conducted with the Cerro Tololo Inter-American Observatory (CTIO) Blanco 4 m telescope to obtain images in *UBVRI* with a pixel scale of $0\farcs27$ and point spread functions between $1''$ and $1\farcs5$. They used images from the CTIO 0.9 m and the Lowell 1.1 m for additional (color) calibration. Internal photometric errors are estimated to be $\lesssim$ 5% for massive stars (M$\gtrsim$ 20 $M_\odot$). Massey et al. (2007) found that their photometry matches that of Bianchi et al. (2001) from HST. The Massey et al. (2007) photometry, however, includes more photometric bands, and provides better detections at the brightest end than either Bianchi et al. (2001) (where HST saturates) or de Blok & Walter (2006).

To obtain absolute magnitudes, we subtract a distance modulus of 23.45 and apply a reddening correction as derived from Efremova et al. (2011). They found a total E(B-V) = 0.41 ± 0.15 for Hubble V and E(B-V) = 0.36 ± 0.16 for Hubble X. This includes a Milky Way foreground component of E(B-V) = 0.22 with R_V = 3.1 plus an internal redding component with an extinction curve similar to that of 30 Doradus in the Large Magellanic Cloud with $R_V \sim 2.68$ (Misselt et al. 1999), resulting in $A_V \sim 1.19$ and $A_V \sim 1.05$ for Hubble V and X, respectively.

For the most luminous stars, we interpolate from main sequence isochrones of ~ 6 Myr (Girardi et al. 2002) with metallicity ~ 0.4 $Z_\odot$ to obtain bolometric magnitudes. These stars are brighter than $M_V \sim -4.3$, representing the OB population that will dominate ionization and any stellar wind input in the region (Cox 2000). For main sequence stars and the measured magnitude M_V, M_{bol} is interpolated from the isochrones and used to calculate the bolometric luminosity:

$$L_{bol} = 10^{(4.75-M_{bol})/2.5}\ \mathrm{L}_{\odot}\,. \quad (4.1)$$

From bolometric luminosities, we can then approximate how many ionizing photons are coming from the stars.

$$\mathbb{N}_{Lyc} \simeq 7.2 \times 10^{43} L_{bol} - 4.4 \times 10^{48}\ s^{-1} \quad (4.2)$$

for O to early B-type stars, where $\mathbb{N}_{Lyc}$ is the number of ionizing photons, and L_{bol} is expressed in units of $\mathrm{L}_{\odot}$ (Vacca et al. 1996).

Some of the bright sources, both in the Massey et al. (2007) and Bianchi et al. (2001) photometry lists, have inconsistent colors in different bands. These are in the crowded center of the clusters within the H II regions, and we attribute the unlikely photometry to crowding, high-background, source-blending, and differential reddening. The Massey et al. (2007) list includes twelve bright sources in the core of Hubble V, of which seven have normal main-sequence colors, three are redder than expected, and two are very blue even before dereddening. Likewise, of eight bright sources in the core of Hubble X, four are unphysically blue. For the seven OB sources with main-sequence colors Hubble V, the total $\mathbb{N}_{Lyc} \sim 1.7 \times 10^{50}$ s^{-1}; for the four in Hubble X $\mathbb{N}_{Lyc} \sim 10^{50}$ s^{-1}.

We can also derive the number of ionizing photons from Hβ. We derive $\sim 30 \times 10^{49}$ s^{-1} for Hubble V and $\sim 25 \times 10^{49}$ s^{-1} for Hubble X, corresponding to 6 and 5 O4 stars, respectively. When compares to the number of ionizing photons derived from photometry, it indicates that the objects with inconsistent colors account for approximately half of the total ionizing radiation.

4.2.3 Mapping dust and gas

We use broad band IR data from the Spitzer Space Telescope (*Spitzer*) (Werner et al. 2004) Infrared Array Camera (IRAC; Fazio et al. 2004) and Multiwavelength Imaging Photometer for *Spitzer* (MIPS; Rieke et al. 2004) and from the Photodetector Array Camera and Spectrometer (PACS) and the Spectral and Photometric Imaging Receiver (SPIRE) aboard the *Herschel* Space Observatory (*Herschel*; Pilbratt et al. 2010). IRAC (3.6-24 μm) and MIPS (24-70 μm) images were taken as part of "The Spitzer Infrared Nearby Galaxies Survey" (SINGS; Kennicutt et al. 2003) and obtained through the NASA/IPAC Infrared Science Archive (IRSA[2]). Reduction of MIPS images is described by Bendo et al. (2012). Herschel FIR and submm maps were obtained and reduced as part of the Dwarf Galaxies Survey (Madden et al. 2013) with data reduction described by Rémy-Ruyer et al. (2013). These broad band maps are combined to produce a map of the dust content of the galaxy.

A background subtraction is applied to *Spitzer*/IRAC, *Spitzer*/MIPS and *Herschel*/ PACS maps. To do so, a median value is estimated from the distribution of background pixels fitted by a Gaussian and subtracted from the maps. Given the low Galactic latitude

[2] http://irsa.ipac.caltech.edu

of NGC 6822, our SPIRE maps are strongly affected by non homogeneous emission coming from Galactic cirrus (Galametz et al. 2010). After masking the emission associated with the galaxy (pixels above 1σ detection in the three SPIRE bands), the cirrus emission is modeled in each map using a Levenberg-Marquardt least-squares 2-D fit with a 3rd order polynomial (we use the function *mpfit2dfun.pro* of the IDL software) and removed from the maps. *Spitzer* and *Herschel* maps (from 3.6 μm to 350 μm) are then convolved to the resolution of SPIRE 500 μm (namely 36″, ~ 85.8 pc) using the convolution kernels of Aniano et al. (2011). The phenomenological SED fitting procedure of Galliano et al. (2011) is finally applied to the 3.6 to 500 μm dataset on a local basis in order to derive a dust mass map of NGC 6822. In this model, the distribution of starlight intensities per unit dust mass is approximated by a simple power law (Dale et al. 2001). The dust size distribution and composition is considered to be uniform across the galaxy. The old stellar population and the dust grains (composed of Polycyclic Aromatic Hydrocarbons, carbon grains, and silicates) are the sources of the IR-to-submm emission. Amorphous carbon grains are chosen to model the carbon dust. Using standard graphitic grains instead would yield higher dust masses, as shown in Galliano et al. (2011). The stellar contribution to the mid-IR is also modeled using a spectral library synthesized using the stellar evolution code PEGASE (Fioc & Rocca-Volmerange 1997). This SED modeling procedure, from background subtraction and convolution steps to the resolved fitting technique, is further detailed in Galametz et al. (2013) where they model the star-forming region N 159 in the LMC.

To assess the neutral gas content, the gas into which each H II region is expanding, we use an H I moment map of NGC 6822 provided by de Blok & Walter (2000). The beam sizes 42″ × 12″, oriented with the long axis approximately north-south. The native map is in units of Janskys per beam. We first convert to a map of integrated intensity ($W_{\rm H\,I}$) in units of K km s^{-1}, multiplying pixel values by 1190.5 K (Cannon et al. 2006) and 1.6 km s^{-1} to account for channel separation (zero-spacing correction; de Blok & Walter 2006). We then covert to number column density using the relation $N_H(\mathrm{H\ cm^{-2}}) = 1.82 \times 10^{18}\ W_{\rm H\,I}\ \mathrm{K\ km\ s^{-1}}$ (Bernard et al. 2008) and to mass column density multiplying by the atomic mass of hydrogen. We find the total mass of H I in circular apertures around each our two regions and convert to density by dividing by the volume of a sphere. The low resolution of the map and likely clumpiness of the gas means that the resulting estimate, approximately the same for both regions, $n_{\rm HI} > 20$ cm^{-3}, must be taken as a lower limit. For a detailed discussion of the ambient medium density see Section 4.5.2.

4.2.4 Ionized gas density

We use [S III] maps in 18 and 33 μm to determine the density of the ionized gas. These two ionized gas cooling lines are dipole forbidden and have approximately the same excitation energy, such that the ratio of the lines is relatively insensitive to temperature for $T_e \sim 10^4$ K. The critical densities, at which collisional de-excitation with electrons becomes important, are different. This line ratio is sensitive in the range $n_e \sim 10^2$-10^4 cm^{-3}, appropriate for the center of H II regions.

We use observations of these two lines from *Spitzer*'s Infrared Spectrograph (IRS

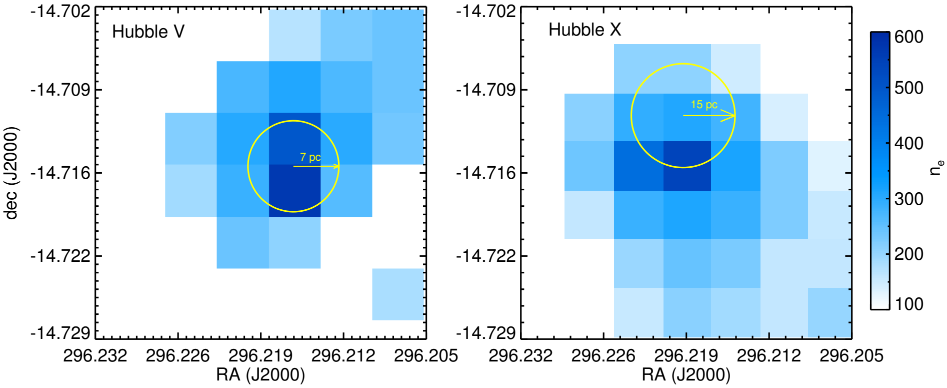

Figure 4.5 – Electron densities for Hubble V (left) and Hubble X (right) derived from [S III] maps in 18 and 33 μm. The circles indicate the same area as in Figure 4.1 and 4.3.

Houck et al. 2004). Observations were performed on September 25th, 2010 (AORkey 9478400), mapping a section of NGC 6822 with the *long-low* module (14-38 μm, spectral resolution $\lambda/\Delta\lambda \approx$ 57-126). The bad pixels in the exposures were first cleaned using the `IRSCLEAN`[3] algorithm. The images were then imported into the spectral mapping software CUBISM (Smith et al. 2007) and further bad pixel cleaning was performed by using the backtracking tool. Finally, we extracted the map of the spectral lines [S III] 18.7, 33.5 μm using CUBISM. Since these lines are isolated and the spectral continuum is fairly simple, we considered a flat continuum for CUBISM to compute the continuum-subtracted line intensity at each position in the map. The spatial resolution of these maps is difficult to know precisely because of the projection of the dispersion axis in the slit, but it should be close to $\sim$ 4″ and $\sim$ 7″ at 18.7 μm and 33.5 μm respectively. We convolve both images to matching resolutions of $\sim$ 7.″5 and regrid to matching pixels of 6″ × 6″ from unaligned native 5″ × 5″ pixels. We take the ratio of 18/33 μm in each pixel and convert to number density, appropriate for an H II region, using a conversion as derived in Dudik et al. (2007). Derived density maps are shown in Fig. 4.5. The average ionized gas density in both regions in the center of the region is $n_e \sim 450$ cm^{-3} for Hubble V and 300 cm^{-3} for Hubble X.

4.3 H II region expansion

The expansion of an H II region has been studied by many authors: Spitzer (1978) studied the expansion due to the effects of overpressure caused by the ionization and heating of the H II region; Castor et al. (1975) considered the mechanical energy of the stellar winds as a main driving mechanism; and Krumholz & Matzner (2009) took into account the

[3] http://irsa.ipac.caltech.edu/data/SPITZER/docs/dataanalysistools/tools/irsclean

Table 4.1 – Properties of Hubble V and Hubble X

	Hubble V	Hubble V
L_{bol} [10^5 $L_\odot$]	48	31
$\mathbb{N}_{Lyc}$ [10^{49} s^{-1}]	30	25
Age [Myr]	< 4	< 4
Radius [pc]	7	15
n_e [cm^{-3}]	450	300
n [cm^{-3}]	61	52
q_{obs} [cm s^{-1}]	1.1×10^8	3.1×10^7
q_{mod} [cm s^{-1}]	1-4 $\times 10^7$	1-4 $\times 10^7$
$M_{\rm H\,II}$ [$M_\odot$]	2.1×10^3	2.7×10^3
M_{dust} [$M_\odot$]	9×10^2	1.1×10^3
M_{tot} [$M_\odot$]	6.2×10^5	7.7×10^5
12 + log(O/H)	8.37 ± 0.09	8.19 ± 0.16

pressure of the radiation on the gas. Independent of the driving mechanisms, analytical models can be used to constrain physical properties of H II region. At a given density of the surrounding medium, each model predicts the radius of the H II region, i.e. the distance of the ionization front from the star, as a function of time. Given two of the three parameters (density, radius, and age), theory allows us to derive the third unknown. We describe hereafter three analytical models and their application to the case of Hubble V and X.

4.3.1 Analytical models

In the simplest scenario of evolution of the ionization front in a uniform gas, the equilibrium solution (where recombination and ionization of hydrogen balance) is known as the Strömgren sphere. The inside of such an H II region has an inner temperature and pressure higher than the surrounding gas, due to ionization, causing a shock to propagate through the medium that sweeps up material into a dense, neutral shell. As the H II region expands, the density inside the H II region slowly drops, requiring fewer photons to keep the gas ionized. The extra photons lead to an increase in the ionized gas mass, following the Spitzer (1978) analytic solution.

However, there are some complications to this picture. High mass stars have stellar winds, and their importance for the expansion of an H II region has been studied by Castor et al. (1975) and Weaver et al. (1977). The wind expands driving a strong shock into the ambient ISM, sweeping it up into a dense neutral shell. The shocked gas is slowed down by the presence of an ambient medium and the "new" stellar wind material now has a

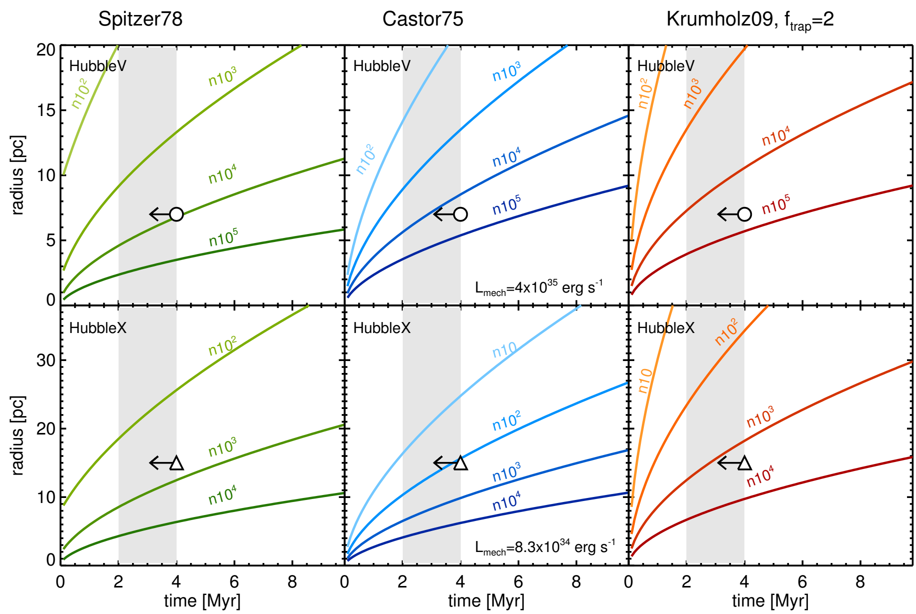

Figure 4.6 – Analytic expansion of H II region radius vs. time for parameters suitable for Hubble V (top row, open circle) and Hubble X (bottom row, open triangle). We compare predictions of three theories: pressure-driven H II regions (Spitzer 1978, left column), wind-driven bubbles (Castor et al. 1975, center column), and radiation pressure-driven shells (Krumholz & Matzner 2009, right column). For each case we show lines calculated with number density of the ambient medium n = 10, 100, 1000, 10^4, 10^5 cm^{-3}. The ages of the stellar cluster are indicated by gray shading.

velocity higher that the already shocked one creating a reverse shock. Such a structure is often referred to as energy-driven, adiabatic wind bubble.

More recently, the importance of radiation pressure in the first phases of H II region expansion, especially those powered by many OB stars, has been stressed both theoretically (Krumholz & Matzner 2009) and observationally (Murray & Rahman 2010). This model has received further impetus by recent studies that show that stellar winds from high mass stars are not as strong as previously thought and that (at least for a population of H II regions) the main driver cannot be the stellar wind (Najarro et al. 2011, Matzner 2002) .

4.3.2 Comparison to observations

Each of these theories for the expansion of H II regions predicts the size as a function of time. The results of these dynamical models can be compared to the observations. We do so for Hubble V and Hubble X in Figure 4.6. The radius of each H II region comes from the Hα maps (circles in Figure 4.1 and 4.3) and the age is the upper limit from the stellar population analysis of Bianchi et al. (2001). These are summarized in Table 4.1. For the Castor et al. (1975) solution we need an estimate of the mechanical luminosity of stellar wind. We derive this using the Vink et al. (2000) mass loss recipe at metallicity 0.4 $Z_{\odot}$ for each identified massive star, as mentioned in Section 4.2.2. We estimate the total L_{mech} as the sum of the contribution of each star. We derive $L_{mech} = 4 \times 10^{35}$ ergs^{-1} for Hubble V and 8.3×10^{34} ergs^{-1} for Hubble X. For the Krumholz & Matzner (2009) solution f_{trap} is the free parameter representing how many times a photon can be used, or how much momentum each photon can deposit into the gas each time it scatters. We use $f_{trap} = 2$, the preferred value in radiation-hydrodynamic simulations of Krumholz & Thompson (2012, 2013). The parameter f_{trap} is important for very luminous clusters, but in the case of our two H II regions, it does not have much influence on the result.

Figure 4.6 shows the predictions of the theoretical models applied to our regions. For adopted ages of 2-4 Myr (see Section 4.2.2 and 4.4.2) and depending on the model, we infer ambient medium densities between 10^4 and 10^5 cm^{-3} for Hubble V, and between 100 and few 10^3 cm^{-3} for Hubble X. We note that for Hubble V, a density of $\sim 10^3$ cm^{-3} is only allowed if the age is substantially less than 1 Myr (Figure 4.6).

4.4 Diagnostic diagrams

The BPT diagram is a useful tool to diagnose emission line origins observed in external galaxies and to distinguish star-forming galaxies dominated by H II regions from active galactic nuclei (AGNs). A BPT diagram consists of emission line pairs of forbidden lines over recombination lines, which are indications of ionization per unit volume. The line ratios [O III]/Hβ versus [N II]/Hα are particularly useful because the wavelengths in each line ratio pair are similar thus insensitive to foreground extinction, and these emission lines are bright (Veilleux & Osterbrock 1987). Individually resolved H II regions form a narrow and well defined sequence of [O III]/Hβ and [N II]/Hα ratios in such plot, while regions ionized by a power-law ionizing spectrum, such as AGNs, are offset (Groves et al. 2004). An H II region's properties, such as density and metallicity, will change the region's location within this narrow sequence on the BPT diagram.

Brinchmann et al. (2004) found from the SDSS that unresolved star-forming galaxies in the local universe fall along the same narrow sequence as individually resolved H II regions. Detailed studies of nearby H II regions provide local analogs to star formation sites in distant galaxies. Therefore, it is important to understand physical processes involved in determining H II region locations along the sequence in BPT diagrams and their relation with the whole star forming galaxies. Chapter 5 and 6 studied how an increase of the environment pressure and the H II regions models affect the location of a galaxy on the diagnostic diagram, while Kewley et al. (2013a) and Kewley et al. (2013b) analyzed the evolution of galaxies on the BPT plot with redshift taking into account both star-forming and AGN galaxies.

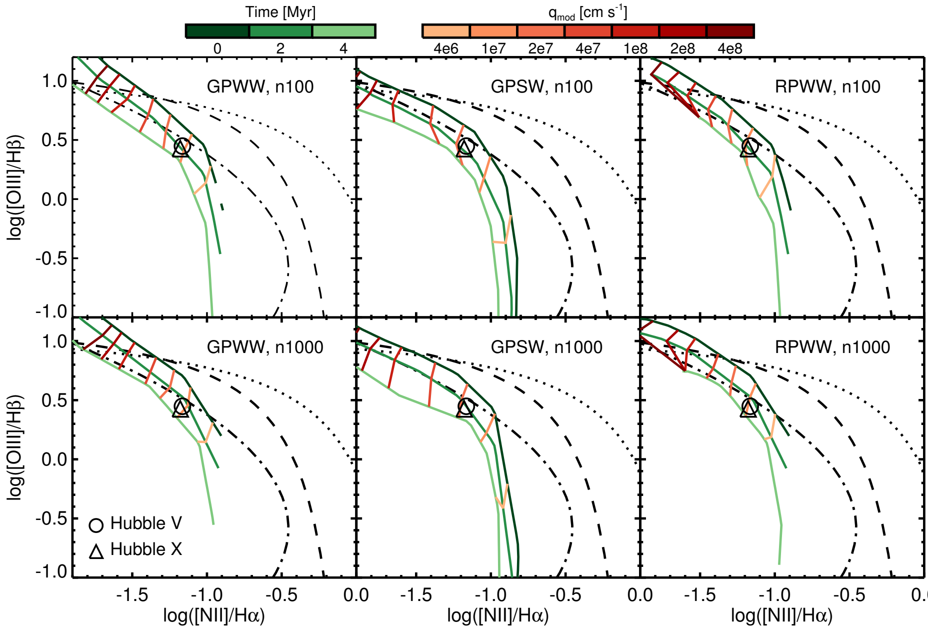

Figure 4.7 – BPT diagram for the photoionization models with initial densities 100 (top row) and 1000 cm^{-3} (bottom row): gas pressure with weak winds (GPWW) on the left, gas pressure with strong winds (GPSW) in the center, and radiation pressure and weak winds (RPWW) on the right. We evolve the models from 0 to 4 Myr (green colors) and we show them with lines of constant q_{mod} parameter (orange). Hubble V and Hubble X integrated measurements are shown as filled circle and square respectively. The dashed line is the Kauffmann et al. (2003) line, an empirical separation of star forming galaxies and AGN based on SDSS galaxies. The dotted line is the Kewley et al. (2001) theoretical limit for star forming galaxies. The dot-dashed line is a fit to the star forming galaxies from the SDSS galaxies Brinchmann et al. (2008).

4.4.1 Spectral synthesis and photoionization models

To investigate the physical properties of Hubble V and X, we construct photoionization models in the same fashion described in Yeh et al. (2013). We briefly describe our model parameters in this paper, for more details we refer readers to Yeh et al. (2013).

We generate a population of static, single H ii regions with a wide range of luminosities and sizes. First we use the stellar population synthesis code Starburst99 (Leitherer et al. 1999) to generate coeval star clusters' spectra of age 0 to 6 Myr, employing the Geneva standard evolutionary tracks (Charbonnel et al. 1996, Schaerer et al. 1993b,a, Schaller et al. 1992) with 0.4 $Z_{\odot}$, and Lejeune-Schmutz (Lejeune et al. 1997, 1998, Schmutz 1998) stellar atmospheres. We then feed the Starburst99 spectra into Cloudy 13.00, last described by Ferland et al. (2013), as the ionizing source in the center of each pseudo H ii region, which is spherical and in force balance. We adopt Cloudy pre-stored

ISM dust grain size distribution and fix the abundances at 0.4 $Z_\odot$[4], with the same gas phase abundances as Dopita et al. (2000). Number density of the hydrogen nuclei at the inner radii of H II regions is fixed at 100 and 1000 cm^{-3}, with the total luminosity of continuum spectra 10^{34} to 10^{46} erg s^{-1} in 0.2 dex steps. Outputs of the integrated luminosity of Hα, Hβ, [O III], and [N II] are recorded for the gas pressure weak wind (GPWW) model, gas pressure strong wind (GPSW) model, and radiation pressure weak wind (RPWW) model (Chapter 5).

The GPWW model are filled Strömgren spheres with uniform gas pressure, comparable to the Spitzer (1978) analytic model. The GPSW model produces regions with a large "voids" in the center filled with hot and diffuse stellar wind gas; ionized gas is confined to a thin shell between the stellar wind bubble and the ionization front, aimed at reproducing the Castor et al. (1975) solution. Finally, the RPWW model represents H II regions of radiation pressure-driven ionized shells, in which radiation pressure is the dominant mechanism for shell expansion and stellar winds are negligible, as described by the Krumholz & Matzner (2009) analytic solution. For detailed discussion and implications of each model, see Chapter 5 and 6.

Figure 4.7 shows results of the GPWW, GPSW, and RPWW model in the BPT diagram for initial densities of 100 and 1000 cm^{-3}. The plot shows the outcome of the models depending on age of the stellar population and on the ionization parameter, q_{mod}. The ionization parameter q is the ratio of the ionizing photon flux to the gas density. It gives an indication of the degree of ionization of an H II region and is defined as

$$q = \frac{\mathbb{N}_{Lyc}}{4\pi R^2 n_e}, \tag{4.3}$$

where R is the radius of the H II region and n_e is the electron density. We evaluate the ionization parameter expected from the models, q_{mod}, at the ionization front radius of each simulated H II region. For the electron density, we use the density of the inner shell for models GPWW and GPSW because the density structure for the set of parameters used does not change significantly. For RPWW models we use the density of the shell at the ionization front as predicted by the models, which is usually higher than the initial one due to radiation pressure piling material up towards the ionization front (Draine 2011, Yeh & Matzner 2012).

4.4.2 Results

The GPWW, GPSW and RPWW photoionization models have some common features (Dopita et al. 2000, Kewley et al. 2001, Levesque et al. 2010). The age of the stellar population causes the [O III]/Hβ ratio to shift down with increasing age. Ages larger than 4 Myr make the models drop dramatically because the most massive stars move out of the main sequence. The ionization parameter increases from right to left on the plot. The metallicity has the effect of shifting the models towards lower [N II]/Hα values (see also

[4] We scale the abundances linearly for all elements with the exception of helium, nitrogen and carbon, for which we adopt the scaling relations in Dopita et al. (2006a).

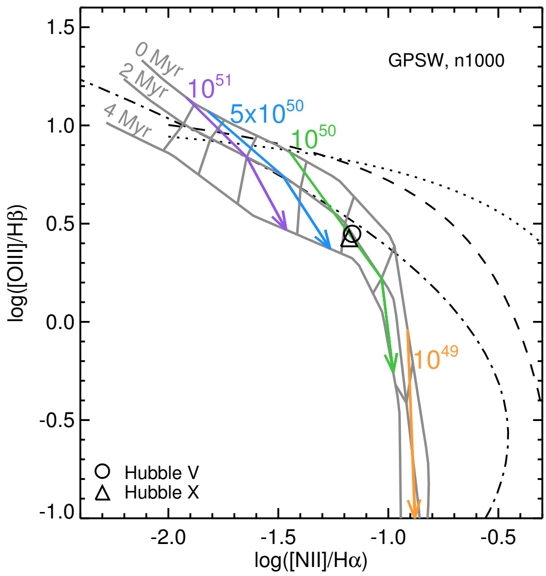

Figure 4.8 – Predicted evolution in time of H ii regions on the BPT diagram. Gas pressure with strong winds (GPSW) grid models are in grey. Arrows indicate increasing time evolution for H ii regions with number of ionizing photons from 10^{49} to 10^{51} s^{-1}. Other lines and symbols are as Figure 4.7.

Figure 6.3 and 6.4). The increase of the density in which the H ii region expands has only small effects on the location of the models in the plot. GPWW and RPWW have very similar results in terms of shape of the overall models with one main difference in the ionization parameter: at a give location, the q_{mod} of the GPWW is systematically higher than q_{mod} of the RPWW by about a factor 2. As expected, GPWW H ii regions are systematically smaller, therefore have higher q_{mod}, than the RPWW ones. As also visible in Figure 4.6, radiation pressure acts as extra force added to the gas pressure driven expansion of the H ii region.

Figure 4.7 also shows the location of our two H ii regions. Despite the different surrounding densities, both H ii regions fall in a very similar location of the BPT diagram. All three models can reproduce the location of the observed regions with fairly similar ionization parameters in the case of gas pressure models and with slightly smaller q values for RPWW model. We discuss this further in Section 4.5.3. We derive q value for those H ii regions of 1-4×10^7 cm s^{-1} for gas pressure models and 4×10^6-10^7 cm s^{-1} for radiation pressure models. The age is restrictd to 2-4 Myr in all models.

As an H ii region ages and expands, the ionization parameter changes. While it is straight forward to see the trend with age on a grid of models, predicting how the ionization parameter changes is not obvious, because it depends on the radius of the expansion and on the density structure created by the H II region. We show an example of our prediction for the evolution of an H II region in Figure 4.8. At a fixed number of ionizing photons, we calculate the radius according to the analytic solutions described Section 4.3. We use the appropriate density at the ionization front as found in the photoionization models (important for the RPWW models) to calculate the ionization parameter that gives the BPT diagram location. The evolutionary tracks predict that H II regions move on the BPT diagram from high [O III]/Hβ and low [N II]/Hα values towards lower [O III]/Hβ and a fixed value of [N II]/Hα that will depend on the metallicity. In order to populate the top part of the diagram, H II regions must be formed by massive stars, to have enough ionizing photons to excite the [O III], and they must be young. When comparing to Hubble V and X, we find again that all the derived parameters (Table 4.1) are consistent with the expected values from Figure 4.8.

4.5 Discussion

In Sections 4.3 and 4.4, we have illustrated unidimensional analytical models and photoionization models for the specific case of Hubble V and X. We expect that those two H II regions are good analogues of H II regions dominating the emission of SDSS galaxies. We connect the information derived from two single cases to the more general trend of the star forming galaxies. Before doing so, we discuss here the physical parameters that we have constrained using the combined efforts of observations and theory.

In order to assess the evolution of the H II region and its physical conditions, it is important to disentangle the degeneracy between age and density of the medium. Consider a star or stellar cluster of known ionizing photons with an observed radius r. Such a radius is the result of the expansion of the H II region in time into its surrounding medium of density n. If we can derive one of the two parameters, we know the other. We discuss here how we derive a tighter constraint on the age of the H II region using the photoionization models, and we prove that the ambient densities derived from observations are lower limits.

4.5.1 Age

Bianchi et al. (2001) used photometric studies of the two clusters to construct H-R diagrams. They derive an upper limit on the age of the stellar cluster of 4 Myr by comparing the data with stellar evolution isochrones. Supporting evidence for a young age comes from the lack of supernovae signature. Shocked gas and H II regions are clearly separated in the BPT diagram, with shocked gas being on the top right part of the plot (Groves et al. 2004). We do not find any indication of shocked gas in the two fields. Considering a single burst of star formation, SN explosions happen after about 3.5 Myr. The lack of SN support that our two clusters have an age less than 3.5 Myr.

We show in Figure 4.7 a set of photoionization models. We can assume that both Hubble V and X come from one single burst of formation, then independently of the model used to describe the driving mechanism of the H II region, both star-forming regions are less than 4 Myr old.

We derived a relatively strong constraint on the age of the stellar population using two different methods. We note that while the isochrone methods are unable to distinguish an age less than 4 Myr, photoionization models together with the BPT diagram give a more precise estimate. Optical lines are very sensitive to the hard radiation coming from high mass stars which evolve very fast to Red supergiant and/or Wolf Rayet star. As a result the BPT plot becomes a more sensitive tool to determine stellar age than isochrones on the H-R diagram.

4.5.2 Density of the ISM

The gas-to-dust ratio is calculated by finding the total H I mass and total dust mass over the main body of the galaxy. We perform aperture photometry over a 440″ radius (centered at ra = 296.208, dec = −14.778 in degrees J2000) on the H I column density map and dust mass map discussed in Section 4.2.3. The total H I mass over this area is $M_{\rm H\,I} \sim 6 \times 10^7$ M$_\odot$, assuming a distance of 490 kpc and adding the contribution of Helium. The total dust mass, using the amorphous carbon model, is $M_{dust} \sim 8.6 \times 10^4$ M$_\odot$. This results in a gas-to-dust ratio of approximately 700 by mass, neglecting contributions from H_2 and trace species. The inherent assumption is that the gas-to-dust ratio is equal to the one measured for the galaxy as a whole. Although dust properties are affected in H II regions (Salgado et al. 2012) causing the value of the gas-to-dust ratio to decrease, the mean field is dominated by the swept up shell, not the ionized gas mass.

We select an circular region around the sources of radius 42 pc, that is the smallest region we can select: the beam size of the 500 μm maps is 12″ corresponding to ∼ 28.5 pc at the source distance. From the dust maps, we calculate the total mass in dust, $M_{dust} \sim 9 \times 10^2$ M$_\odot$ and 1.1×10^3 M$_\odot$, respectively for Hubble V and Hubble X. By multiplying by the gas-to-dust ratio, we derive the total mass in the region for Hubble V M_{tot} is $\sim 6.2 \times 10^5$ M$_\odot$ and for Hubble X $\sim 7.7 \times 10^5$ M$_\odot$. We calculate the total mass of the ionized gas from the number of ionizing photons and the density of the ionized gas (Section 4.2.4 and Figure 4.5) obtaining for the two H II regions, respectively, $M_{\rm H\,II} \sim 2.1 \times 10^3$ and 2.7×10^3 M$_\odot$. The ionized gas densities of ∼ 300-450 cm^{-3} measures the dense shell of swept up ionized material; it is not a direct measure of the density of the ambient medium. In terms of mass, the ionized gas has a minor contribution to the total budget. Finally, we derive the density of the ISM by dividing the total mass by the volume of the sphere with radius 42 pc. We get a Hydrogen density $n_{\rm H} \sim 61$ cm^{-3} for Hubble V and $n_{\rm H} \sim 52$ cm^{-3} for Hubble X. Note that these are higher than the values estimated directly from H I in Section 4.2.3.

The densities derived from observations are lower limits, and Figure 4.6 indicates that they are lower than necessary to confine the expanding H II regions to the observed radii. In the previous section, we show via two independent methods that the regions cannot be older than 4 Myr, most probably ∼ 2 Myr. With this estimate in mind we can go back to Figure 4.6 and derive the density of the medium surrounding the H II regions. Almost independently of the expansion model one considers, Figure 4.6 indicates that the density in both regions must be higher than the values derived with the dust maps.

In the case of Hubble V, the discrepancy between the predicted and estimated values of the ISM density is of a factor of 150 to 1000 (depending on the models), while in the case of Hubble X is smaller. For Hubble X the expected density of the ISM is between 100 and 800 cm^{-3}, for Spitzer (1978) and Castor et al. (1975) models, and up to few thousands for Krumholz & Matzner (2009). Therefore, the values of the density of the medium derived from observations are a factor of 2 to 16 lower than predicted by the first two analytical models. Such a difference between the two H II regions might be due to the morphology. The analytical models are unidimensional, suitable for spherical and confined H II regions. It might explain the better fit for Hubble X, that has an almost spherical appearance. While looking at the optical image of Hubble V and the location of the dust clump, it seems indicating that the H II region is open on one side and that gas is leaking out in a champagne flow.

Despite the discrepancies between models and observations, we can deduce some important points. First, Hubble V must be in the vicinity of a high density clump on scales smaller than those measured that stops the expansion on one side and that generates the strong emission lines. Second, the density derived from observations is a lower limit indicating that we are possibly missing dust in the detection, indication that the IR data is dominated by the emission from warm dust in the PDR and that much of the dust in the swept up shell is very cold and escapes detection with Herschel.

4.5.3 Ionization parameter

We derive two independent estimates of the ionization parameter q, one from observations q_{obs} that can be compared with the values derived from models, q_{mod} in Section 4.4.1. We fix the number of ionizing photon flux to the observed value in both observational and theoretical estimates. We use the values of $\mathbb{N}_{Lyc}$ as listed in Table 4.1.

To derive q_{obs}, we use the radius of the region as seen from Hα. We derive the electron density from [S III] maps in 18 and 33 μm as described in Section 4.2.4 and shown in Figure 4.5. For Hubble V the average electron density within the bubble is $\sim$ 450 cm^{-3}, while in Hubble X is $n_e \sim 300$ cm^{-3}, giving q_{obs} values of 1.1×10^8 and 3.1×10^7 cm s^{-1} respectively. Figure 4.7 shows the grid of models on the BPT diagram, from which it is possible to see that the ionization parameter is approximately between 1 and 4×10^7 cm s^{-1} for all models. Considering the uncertainties and the assumptions made, we can say that for both H II regions the estimates of the ionization parameter derived from observation and theory are consistent. Both regions have similar ionization state, which is what it is typically found for H II regions in the local universe. However, Hubble V has an observed ionization parameter higher than expected from the models (Section 4.4.2). It could be due to geometrical effects caused by a deviation from spherical of the H II region's shape.

4.5.4 Comparison with SDSS galaxies

Star-forming galaxies and H II regions in the local universe follow the same sequence in the BPT diagram, suggesting that star-forming galaxies can be simplified as a collection

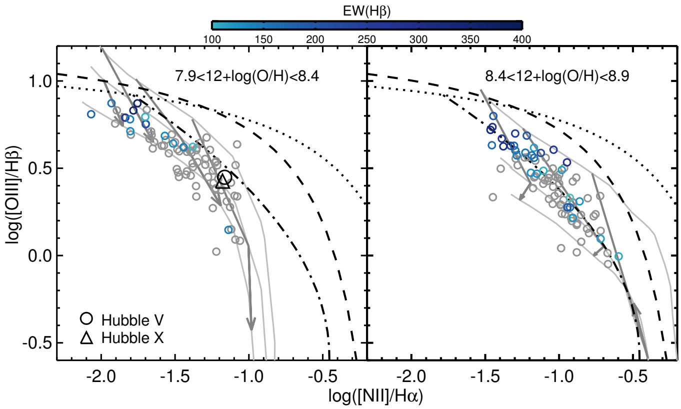

Figure 4.9 – Sub samples of SDSS data on the BPT plot. We selected star forming galaxies from the SDSS catalogue that have a spectrum of a region less than 200 pc in diameter and divided them in two metallicity bins: 12+log(O/H) between 7.9 and 8.4, and between 8.4 and 8.9, corresponding respectively to 0.4 and 1 $Z_{\odot}$. We further divide the sample into galaxies with EW(Hβ) below 100 Å in gray circles, and above 100 Å, color coded according to their EW(Hβ). Models GPWW with 0.4 and 1 $Z_{\odot}$ for ages 0, 2 and 4 Myr are shown together with the self-consistent predictions of evolution of H ii regions in time (grey lines). Hubble V and Hubble X integrated measurements are shown as open circle and square respectively.

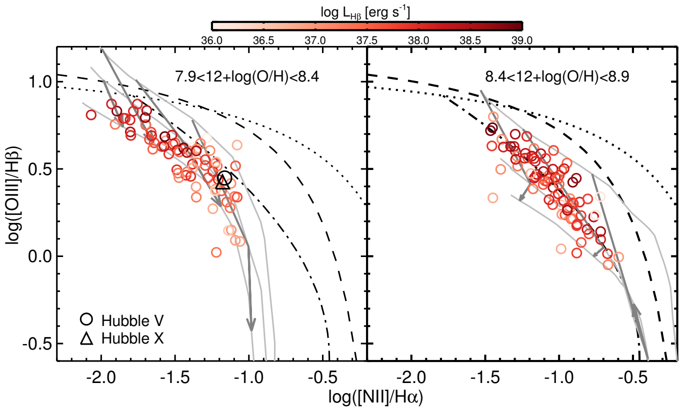

Figure 4.10 – Sub samples of SDSS data on the BPT plot. We selected star forming galaxies from the SDSS catalogue that have a spectrum of a region less than 200 pc in diameter and divided them in two metallicity bins: 12+log(O/H) between 7.9 and 8.4, and between 8.4 and 8.9, corresponding respectively to 0.4 and 1 $Z_{\odot}$. Each data point is color coded according to the logarithm of the luminosity in Hβ. Models GPWW with 0.4 and 1 $Z_{\odot}$ for ages 0, 2 and 4 Myr are shown together with the self-consistent predictions of evolution of H ii regions in time (greylines). Hubble V and Hubble X integrated measurements are shown as open circle and square respectively.

of H II regions. Contamination from warm ionized gas has an influence only on galaxies with low specific star formation rate (Mathis 2000, Brinchmann et al. 2004) that is not relevant for this discussion. In this Section, we compare star-forming galaxies dominated by H II regions with single H II regions based on their location on the BPT diagram.

In Chapter 6 we created synthetic galaxies as collections of H II regions using a population synthesis code aimed at understanding the star forming sequence of galaxies. We generated H II regions according to an initial mass function and a constant star formation rate. We evolved each H II regions according to an analytic expansion models (Spitzer 1978, Krumholz & Matzner 2009) and we predicted their line emission with photoionization models. We found that the main difference between models with low (0.1 $M_\odot$ yr^{-1}) and high (10 $M_\odot$ yr^{-1}) star formation rate is due to the number of massive H II regions formed at each time, and it decides the spread of synthetic galaxies on the BPT diagram. The low star formation case generates galaxies with a large spread on the BPT diagram, while galaxies generated with high star formation rate are more concentrated. It is due to the stochastic nature of star formation: for low star formation rates most of the H II regions formed are powered by relatively late spectral types (eg. $\sim$ O9) that have weak emission lines and a low [O III]/Hβ ratio. Whenever a bright H II region is formed, its light dominates over the entire galaxy and brings the [O III]/Hβ ratio up, causing the spread in values. When the SFR is high, there is always a massive H II region to keep the ratio up, therefore showing no spread on the BPT diagram. In other words, with a constant star formation rate, the most massive and youngest H II region dominates the light of the entire galaxy, with only a weak influence of the underlying old stellar population.

Hubble V and Hubble X are two examples of young and bright H II regions, they are good analogues of the H II regions dominating the emission in star forming galaxies. We compare our single H II regions to a selection of star forming galaxies from the SDSS data. We can also use the information we have on the two H II regions to further validate the way we extrapolate physical information from the diagram. We selected galaxies in the SDSS sample that have spectra of regions less than 200 pc in diameter. In this way, we try to minimize the effect of contamination due to emission from the warm ionized medium. For those galaxies, we take the equivalent width of Hβ (EW(Hβ)) as an indicator of young stellar population. When the EW(Hβ) is $>$ 100 Å then the star formation and light are dominated by a very young population without contamination from an underlying old stellar population. We divide the sample into young sources with EW(Hβ) $>$ 100 Å, and old sources $<$ 100 Å. We further split the sample according to metallicity: $12 + log(O/H)$ between 7.9 and 8.4, and between 8.4 and 8.9 (corresponding to 0.4 and 1 $Z_\odot$); and plot the data on the BPT diagram (Figure 4.9). We find that young sources are systematically shifted towards the top part of the BPT diagram, suggesting that their light must be dominated by massive H II regions. Hubble V and X are located towards the low end of the distribution of young galaxies, indicating the time evolution of such galaxies.

In Figure 4.10 we consider the same sample of star forming galaxies divided into metallicity bins, and show their Hβ luminosity. Even though the trend is not as clear as in the previous plot, there is an indication that galaxies dominated by young H II regions are also the most luminous in Hβ. The luminosity of the emission line Hβ is an indication of the star formation activity in the galaxy because its emission comes primarily from high mass stars present in the galaxy. Therefore, Figure 4.10 confirms that the location of galaxies on the star forming sequence of the BPT diagram is partially due to the presence and age of high mass stars.

From the comparison between single H II regions and star forming galaxies, we can draw the following conclusions. First, galaxies dominated by young H II regions show higher [O III]/Hβ than the older ones and are found systematically on the top left part of the plot, independently of the metallicity and they are generally more luminous galaxies. Second, [N II]/Hα value is mostly dependent on the metallicity that translates the data points on the plot almost rigidly. Third, when compared to the photoionization models, it is clear that the location of the galaxies dominated by young H II regions is due to the combined effect of young age and high ionization parameter. Finally, Hubble V and Hubble X are located at the lower end of the young part of the star forming sequence, indicating that the most massive stellar cluster in blue star forming galaxies tend to be younger than our H II regions.

4.6 Conclusions

We select two very well studied H II region in the nearby galaxy NGC 6822: Hubble V and Hubble X. We use Hβ, [O III], Hα, and [N II] optical emission line images taken with the WFC2 camera from the HST to produce the BPT diagram and to look at the morphology of the two regions. We use photometry from Massey et al. (2007) to characterize the stellar population and the age of the region. Finally, we use broad band IR data to map the dust content that together with the estimates of the neutral gas from H I maps from de Blok & Walter (2000) gives us the gas-to-dust ratio in the galaxy.

We make use of unidimensional analytical models to get a better constrain the density of the medium around each H II region. We consider three theoretical descriptions of the expansion of H II regions: Spitzer (1978) takes into account the overpressure caused by the ionization and heating of the H II region; Castor et al. (1975) the mechanical energy of stellar winds; and Krumholz & Matzner (2009) the radiation pressure on the gas. Given the density of the ISM, each model describes the expansion radius of the ionization front as a function of time. The estimates of the density we derive from the models are few orders of magnitude higher than the observed ones indicating that we might be missing the detection of the very cold dust, probably because overpowered by the warm dust emission.

We test photoionization models for three possible H II region driving mechanisms. We find no major difference between the models. Together with the BPT diagnostic diagram such models are able to confirm the young age of the clusters ($\sim$ 2 Myr) and the ionization state of the regions ($q \sim 10^7$ cm s^{-1}). We created evolutionary tracks on the BPT plot useful to understand general trends in the star forming sequence.

We find many similarities in the two H II regions: they are both young, powered by similar stellar clusters, and have a similar ionization states. However their morphology is strikingly different. The brightest part of Hubble V is expanding in a very dense molecular cloud, $> 10^4$ cm^{-3}. Gas seems to escape towards the South-East part of the object, where the density likely drops and a "champagne flow" begins. Hubble X has a more regular spherical shape and is expanding in a less dense ($\sim 10^3$ cm^{-3}) and more uniform medium.

We compare a selection of SDSS galaxies to models and to Hubble V and X in the BPT diagram. We use the equivalent width of Hβ as an indicator of recent start formation, and the luminosity of Hβ. We find that star-forming galaxies' locations in the BPT diagram is dominated by the few, very bright H II regions, rather than by the numerous dim stars. The location of Hubble V and X suggests that the evolutionary tracks derived from photoionization models are consistent with observations and can be extended to the more general case of star forming galaxies. We suggest that detailed studies of global properties of H II regions will help disentangle the debate on their driving mechanisms.